

Compressibility and Structural Transformations of Aluminogermanate Imogolite Nanotubes under Hydrostatic Pressure

S. Rouzière,* V. Balédent,* E. Paineau, E. Elkaim, T. Bizien, L. Nataf, Y. Pan, and P. Launois



Cite This: *Inorg. Chem.* 2023, 62, 957–966



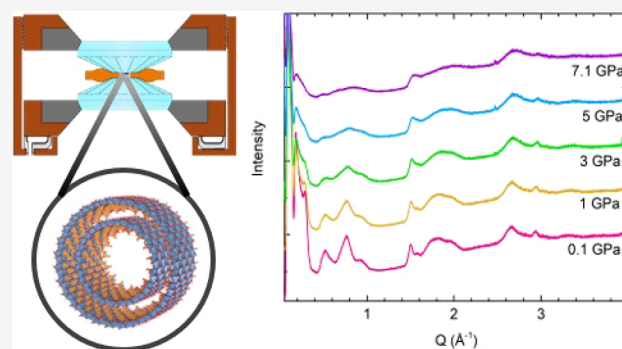
Read Online

ACCESS |

Metrics & More

Article Recommendations

ABSTRACT: We present *in situ* pressure experiments on aluminogermanate nanotubes studied by X-ray scattering and absorption spectroscopy measurements. Structural transformations under hydrostatic pressure below 10 GPa are investigated as a function of the morphology, organization, or functionalization of the nanotubes. Radial deformations, ovalization for isolated nanotubes, and hexagonalization when they are bundled are evidenced. Radial collapse of single-walled nanotubes is shown to occur, in contrast to the double-walled nanotubes. The effect of the transmitting pressure medium used on the collapse onset pressure value is demonstrated. Axial Young's moduli are determined for isolated (400 GPa) and bundled (600 GPa) single-walled nanotubes, double-walled nanotubes (440 GPa), and methylated single-walled nanotubes (200 GPa).



INTRODUCTION

Nanotubes have been iconic objects of major importance in nanosciences and nanotechnologies since the discovery of carbon nanotubes (CNTs) at the beginning of the 1990s. They are promising building nanobricks for many applications¹ such as nanoelectronics,² nanofluidics,^{3,4} and photocatalysis.^{5,6} Moreover, nanotubes can exhibit outstanding physical properties due to their unique anisotropic structure such as, for example, high stiffness of CNTs characterized by an exceptionally high Young's modulus.^{7,8} The structure of nanotubes can be controlled by applying external forces. In particular, the application of pressure may lead to the synthesis of new nanomaterials induced by polygonalization,^{9,10} ovalization, or polymerization.¹¹ For instance, it has been recently shown that the radial collapse at high pressure of CNTs organized in bundles led to the formation of particular two-dimensional (2D) nanostructures of graphene ribbons.¹² Pressure-induced deformations of nanotubes can therefore lead to significant modifications of their electric and mechanical properties.

The excitement around CNTs has recently shed light on metal oxide imogolite nanotubes (INTs), which have been demonstrated to have potential applications in photocatalysis¹³ and selective molecular sieving.¹⁴ Natural imogolite is an aluminosilicate single-walled nanotube with the stoichiometry $\text{SiAl}_2\text{O}_7\text{H}_4$,¹⁵ which was initially discovered in volcanic soils.¹⁶ However, INTs with controlled diameter, morphology, and organization¹⁹ can also be easily synthesized using soft

chemistry.^{17,18} In contrast to CNTs, the strain energy is minimum for specific values of their chiral indices, leading to nanotubes monodisperse in diameter and chirality at the end of the synthesis.^{20,21} Aluminosilicate INTs are single-walled nanotubes made of tetrahedral $[(\text{OH})\text{SiO}_3]$ units on the inner surface sharing oxygen atoms with octahedral $[\text{O}_3\text{Al}(\text{OH})_3]$ units of a curved gibbsite-like framework on the outer surface. Isomorphous substitution of silicon by germanium allows obtaining aluminogermanate INTs with either single-walled (SW) or double-walled (DW) morphology.²² Furthermore, SW-INTs can be made hydrophobic by replacing hydroxyl groups in the inner cavity by methyl moieties,^{23,24} yielding nanotubes of chemical formula $(\text{OH})_3\text{Al}_2\text{O}_3\text{XCH}_3$ ($\text{X} = \text{Si}$ or Ge), which also possess a different chirality.²⁵ In brief, the aluminogermanate INTs family offers a variety of compounds with well-controlled morphology, diameter, and chirality.

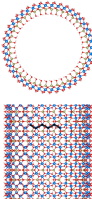
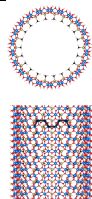
Computational studies have reported a calculated Young's modulus for INTs in the range from 100 to 400 GPa.^{21,26,27} Furthermore, calculations of the frequency values of radial breathing modes (RBM) suggested that INTs are rather soft in

Received: October 28, 2022

Published: January 3, 2023



Table 1. Description of the Aluminogermanate INTs Measured in This Study^a

	SW-GeOH ³⁷	SWb-GeOH ³¹	DW-GeOH ³⁸	SW-GeCH ₃ ²⁵
				
R_{inner} (Å)	13.8	13.8	7.7 ¹ -13.7 ²	8.8
R_{outer} (Å)	20.3	20.3	15.7-21.7	13.6
T (Å)	~8.6	~8.6	~8.6	4.95
Rolling Mode	ZZ	ZZ	ZZ	AC
L (nm)	~100	~100	~100	10
NTs per bundle	< 4	~60	< 4	< 4

^aLegend: (1) inner wall of the double-walled nanotube; (2) outer wall of the double-walled nanotube.

their radial directions,^{21,28} which may induce structural transformations under external stimuli. Molecular dynamics simulations predicted that ovalization of the nanotube's cross-sectional shape can occur when nanotubes are brought close to each other.^{29,30} From an experimental point of view, hexagonalization of SW-INTs was evidenced after desiccation at atmospheric pressure if the nanotubes were assembled in large bundles.³¹ In addition to these deformations, it has been shown that INTs undergo major structural transformations under thermal treatment before recrystallizing into a mullite-like phase at around 1000 °C.^{32–35} Yet, the study of the deformations and structural transformations of INTs under pressure has remained to date an unexplored field.

In this study, we have investigated the pressure-induced structural transformations of aluminogermanate INTs depending on different physical parameters: that is, (i) the morphology, with either single (SW)- or double-walled (DW) nanotubes, (ii) the organization when nanotubes are self-arranged in bundles (SWb), and (iii) the functionality of the inner cavity on methylation (see Table 1). Radial deformations and axial compressibilities of the nanotubes have been measured. We have also evaluated the effect of two different pressure-transmitting media (PTM), Si (silicone) oil and an ethanol/methanol mixture, in relation with the diameter and the affinity of the inner cavity of the nanotube. We have carried out X-ray scattering experiments to probe structural transformations under hydrostatic pressure and X-ray absorption near edge structure (XANES) measurements to probe changes in the local nanotube structure around the Ge atom.

EXPERIMENTAL SECTION

Aluminogermanate Imogolite Nanotubes. Single-walled aluminogermanate imogolite nanotubes with hydroxylated (SW-GeOH) and methylated (SW-GeCH₃) inner cavities were synthesized at $T = 95$ °C by the hydrolysis of chemical precursors with a NaOH solution following the protocol described by Amara et al.²⁴ In contrast, nanotubes with a double-walled shape (DW-GeOH) were obtained using the urea method under hydrothermal conditions ($T = 140$ °C).¹⁸ We wish to emphasize that hydrated aluminum perchlorate was chosen as the aluminum precursor instead of anhydrous salt in order to minimize any risk of exothermic reactions when mixing with water. In

all cases, the mixtures were aged for 5 days, and then the resulting suspensions were dialyzed against ultrapure water, dried at 70 °C, and finally reduced to fine-grained powders. A bundled nanotube sample (SWb-GeOH) was simply obtained by limiting the number of dialysis cycles.¹⁹ Details on the characterizations of aluminogermanate INTs have been reported elsewhere^{19,25,31,36,38} and are summarized in Table 1.

The internal porosity differs according to the nanotube morphology. The inner radius R_i of DW (7.7 Å) is similar to that of methylated SW (8.8 Å) and much smaller than the inner radius (13.8 Å) of hydroxylated SW INTs (see Table 1). It was shown that the rolling mechanism differs between hydroxylated and methylated INTs.²⁵ By analogy with CNTs,³⁹ the structure of INTs can be defined by two integers (n,m) defining the so-called chiral vector in a hexagonal lattice that describes the rolling mode of the nanotube. A rolling mode with ($n,0$) indices corresponds to a “zigzag” (ZZ) arrangement for hydroxylated nanotubes, whereas methylated substitution changes it to an “armchair” (AC) arrangement with a chiral vector (n,n). This induces a different axial periodicity, with periods T of 8.6 and 4.95 Å for hydroxylated and methylated INTs, respectively.

Prior to measurements under pressure, INT powders were dried in an oven for 2 h at 200 °C in order to remove all water molecules within the structure according to previous thermogravimetric analyses.^{31,35,37}

Pressure Measurements. A diamond anvil cell (DAC), equipped with a 1 mm culet diamond, was used to apply pressure. The sample powder was loaded into a copper–beryllium gasket, within a 500 μm diameter and 80 μm thick hole, together with a ruby chip to monitor the pressure using the standard ruby fluorescence calibration.⁴⁰ An ethanol/methanol mixture in 1/4 volumic proportion and silicone (Si) oil (Rhodorsil silicone oil 47 V 1000) were both used as pressure transmitting media (PTM), providing quasi-hydrostatic pressure below 10 GPa.⁴¹ The internal pressure of the diamond anvil cell was determined by fitting the spectral shift of the R1 fluorescence line, resulting in an ±0.1 GPa uncertainty. Measurements were made on ramping up from ambient to the maximum pressure. The ruby line was measured before and after each measurement, and we observed a small drift of the pressure, resulting in an overall uncertainty of the pressure of 5% of the pressure: 0.1 at 1 GPa and 0.5 at 10 GPa. Variation of the width of the sample as a function of the pressure, due to the gasket shrinking, forbid an intensity calibration into absolute units. X-ray scattering patterns are thus presented in arbitrary intensity units. Let us underline that PDMS (C₂H₆O_{Si})_{*n*} molecules in Si oil are unlikely to fit the internal pore of INTs (see Table 1) due to their large gyration radius⁴² ($R_g \approx 2–3$ nm), whereas ethanol (C₂H₅OH), molecular size of

0.44 nm) or methanol (CH_3OH , molecular size of 0.36 nm) molecules do.

X-ray Scattering Measurements. X-ray scattering (XRS) experiments were carried out on two beamlines at the synchrotron SOLEIL (Saint Aubin, France). They were performed on the CRISTAL beamline on a two-circle diffractometer equipped with silicon-strip linear detectors, in the scattering wavevector Q range $0.1\text{--}5\text{ \AA}^{-1}$ with wavelength $\lambda \approx 0.7284\text{ \AA}$ ($Q = \frac{4\pi}{\lambda} \sin \theta$, where 2θ is the scattering angle). Measurements were completed on the SWING beamline at wavelength $\lambda = 1.2398\text{ \AA}$ with a two-dimensional hybrid-pixel detector in the lower Q range $0.05\text{--}1\text{ \AA}^{-1}$.

Broad oscillations on the calculated XRS pattern in Figure 1 are characteristic of the nanotube form factor and are related to the finite

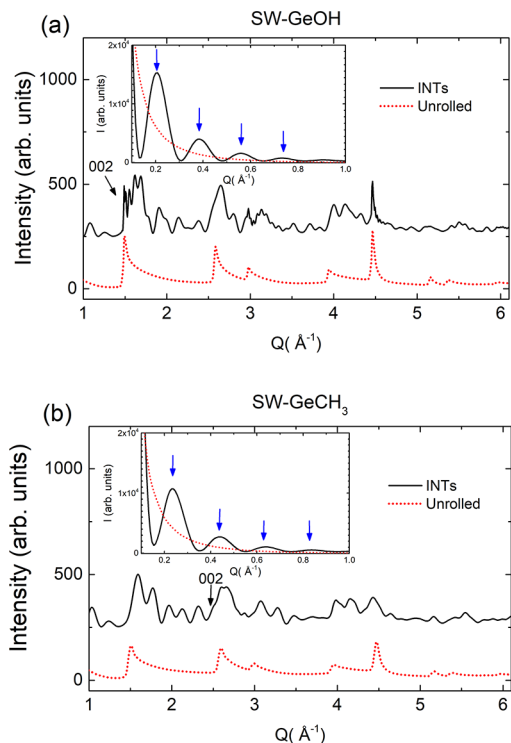


Figure 1. Calculated XRS pattern of a powder of isolated (nonbundled) (a) (22,0) SW-GeOH nanotubes (black curve) and unrolled counterparts (dotted red curve) and (b) (11,11) SW-GeCH₃ nanotubes (black curve) and unrolled counterparts (dotted red curve). The curves are translated vertically for clarity. Blue arrows point toward modulations related to the nanotube form factor, and the 002 asymmetric peak associated with the period T is indicated.

radial tubular dimension of the nanotube, which does not exist for an unrolled nanotube. Modulations below 1 \AA^{-1} give us information about the cross-sectional shape and radial dimensions of the nanotube. Our analysis therefore focuses on their evolution as a function of the pressure, as well as the variation of the broad modulation around 1.8 \AA^{-1} related to the atomic tubular structure. Let us note that, in the case of nanotubes organized in bundles, an XRS pattern below 1 \AA^{-1} is formed of diffraction peaks, instead of broad oscillations, which come from the structure factor of the bundle. Peak positions and widths are then related to lattice parameters and to the number of nanotubes within the bundle.¹⁹ For nanotubes in bundles or nanotubes walls in DW-INTs uncorrelated in position and orientation, modulations at larger Q values ($Q > 1\text{ \AA}^{-1}$) reflect only the nanotube's atomic structure. On the XRS pattern (Figure 1), asymmetric (sawtooth shape) peaks at around $Q_{002n} \approx 1.5, 3.0,$ and 4.5 \AA^{-1} (with $n = 1, 2, 3$), respectively, observed for INTs with ZZ-type rolling mode are associated with the long-range periodic order along the nanotube axis. Note that the axial period T ($T \approx n4\pi/Q_{002n}$) is not determined by the position of the peak

maximum but by the inflection point of its rising edge so as to take into account the finite correlation length.^{25,43} For methylated nanotubes (AC-type rolling mode), the asymmetric peak is located at $Q_{002} \approx 2.5\text{ \AA}^{-1}$, as the axial period is smaller than in hydroxylated nanotubes (see Table 1).

X-ray Absorption Spectroscopy Measurements. X-ray absorption spectroscopy near edge structure (XANES) experiments under pressures of up to 10 GPa were performed at the Ge K-edge ($E_0 = 11.103\text{ keV}$) on the ODE beamline at synchrotron SOLEIL. This beamline uses a dispersive setup in which the beam is focused at the sample region with an elliptically curved Si (111) crystal into a focus spot of $30 \times 30\text{ }\mu\text{m}^2$ (fwhm). This bent crystal also allows fast acquisitions, since an energy range of 435 eV is directly accessible at the Ge K-edge. X-ray absorption was measured by a position-sensitive charge coupled device (CCD) detector (see more details in ref 44). All XANES spectra have been normalized to unity at high energy.

RESULTS AND DISCUSSION

Radial Compression of INTs. XRS measurements of the four different aluminogermanate INTs samples under pressure with the two different PTM are plotted in Figure 2. Changes in the XRS diagrams are observed once the pressure is applied on the four compounds. As detailed in the Experimental Section, pressure-induced modifications of the nanotube cylindrical shape can be assessed by following the evolution of the modulations located at $Q < 1\text{ \AA}^{-1}$ for SW-GeOH, SW-GeCH₃ and DW-GeOH compounds. As illustrated in Figure 3 for SW-GeOH, the intensities of modulations are already modified at the lowest applied pressure in comparison with the *ex situ* measurement at ambient pressure ($P = 1\text{ bar}$). Modulations are strongly decreasing at pressures until $P_c \approx 3.5\text{ GPa}$ with the ethanol/methanol PTM, whereas it occurs at a lower pressure, $P_c \approx 1.8\text{ GPa}$ with the Si oil PTM (Figure 3c,d). Such variation is attributed to modifications of the cross-sectional nanotube shape, from a circular shape to a more or less oval cross-section shape. The ovalization process can be modeled by taking an elliptical cross-section shape,³⁴ as sketched in Figure 4. Our results indicate that the increasingly strong ovalization eventually leads to the radial collapse of the nanotube at a pressure P_c , the low Q vectors ($Q < 1\text{ \AA}^{-1}$) scattering pattern of the flattened nanotube being similar to that of the unrolled (or flattened) nanotube (see Figure 3a,b). The larger critical pressure for the alcohol mixture PTM is attributed to the filling of the tubes by ethanol and methanol molecules, which makes it less radially deformable under pressure. As stated previously, PDMS molecules of Si oil cannot enter the tubes.

Concerning the SW-GeCH₃ sample, evolution of the modulations are similar for both PTM, until their disappearance at about $P_c = 4\text{ GPa}$ (Figure 2). This points out a difference between hydroxylated and methylated SW INTs with respect to the affinity of their inner cavity to alcohol molecules. It suggests that methanol/ethanol molecules enter the hydroxylated inner cavity but not the methylated cavity. Interestingly, SW-GeCH₃ shows a peculiar feature for pressures above P_c with the growth of oscillations at periodic positions $Q \approx 0.175, 0.35, 0.525\text{ \AA}^{-1}$ (see Figure 2). It corresponds to the formation of a lamellar structure with a characteristic distance $d = 3.6\text{ nm}$. Let us note that the formation of a lamellar phase with an interlayer distance of 2.6 nm issued from the thermal collapse of methylated aluminosilicate INTs at 570 K was discussed previously by Zanzottera et al.³³ The authors proposed the formation of patches of layers together with INT portions, acting as spacers and keeping aside the lamellar regions to explain such a large distance d . In our case, we suggest that some SW-GeCH₃ INTs

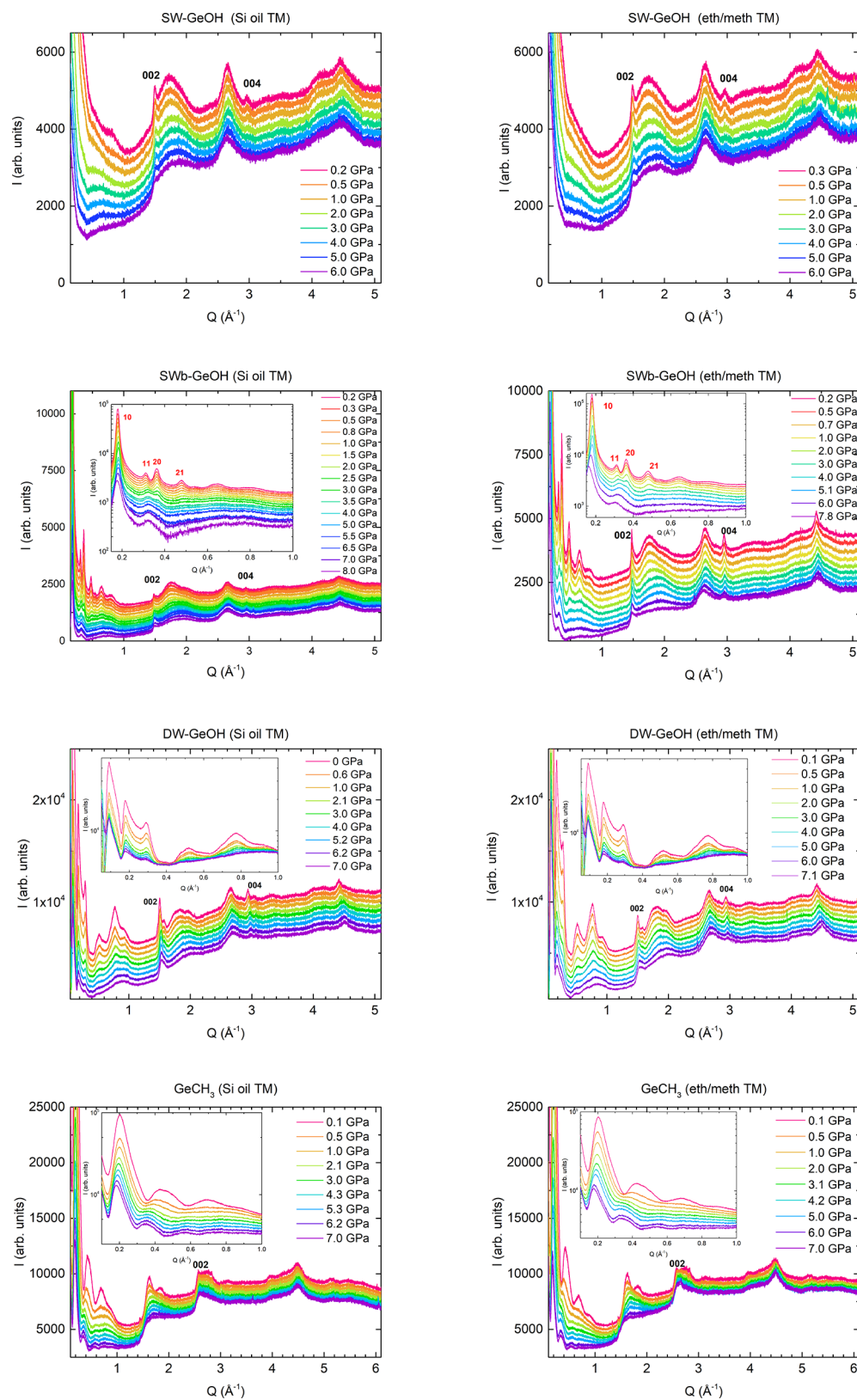


Figure 2. Experimental XRD diagrams (CRISTAL beamline) as a function of the pressure for the four aluminogermanate INTs samples with Si oil (left) and ethanol/methanol (right) PTM. Insets: focus on the low-*Q*-value region 0.1–1 Å⁻¹.

unaffected by the pressure may act as such spacers due to their shorter length and smaller internal pore (see Table 1), in contrast to SW-GeOH INTs, which all undergo a complete collapse mechanism with the application of pressure.

For DW-GeOH nanotubes, some intense modulations are observed between 0.4 and 1 Å⁻¹ (see Figure 2), which come from the interference between the inner and outer tubes.⁴⁵ Experimentally, the intensity of the oscillations gradually

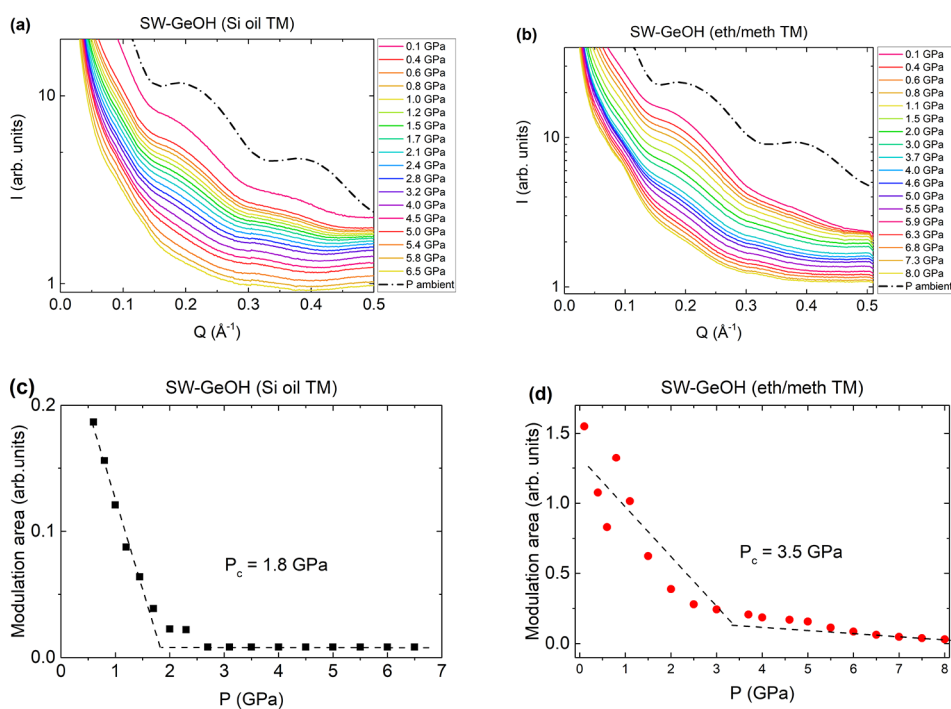


Figure 3. (a, b) Pressure dependence of the intensity of modulations at low Q values (SWING beamline) for SW-GeOH with the two different PTM. The ashed curve corresponds to the experimental curve of nondeformed (cylindrical) nanotubes at ambient pressure. (c, d) Amplitude of the modulation between 0.14 and 0.27 \AA^{-1} as a function of pressure for both PTM. Dashed lines are guides for the eye, and the collapse pressure P_c is defined at their intersection point.

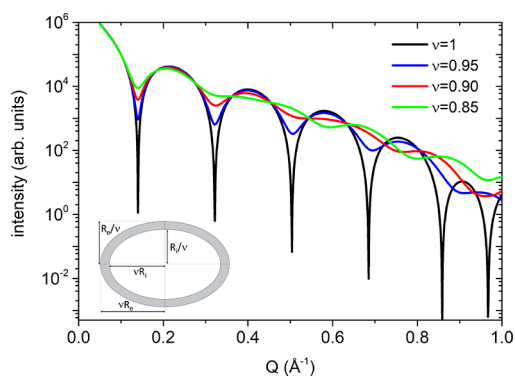


Figure 4. Calculated XRS diagrams of a powder of SW-GeOH nanotubes with an elliptical shape as a function of the elliptical factor ν ($\nu = 1$ corresponds to the case of a cylindrical nanotube).

decreases before vanishing at 6 GPa, without a noticeable difference between the two PTM (Figure 2), which corresponds to variations of diameters related to modifications of the cylindrical cross-sectional shape of the nanotubes. However, a broad modulation centered at $Q \approx 0.9 \text{ \AA}^{-1}$ is still present at the maximum pressure measured of 7 GPa. The corresponding distance is $d = \frac{2\pi}{Q} \approx 7 \text{ \AA}$. It is rather close to the distance between the mean radii of inner and outer tubes of the initial DW-INTs, which is equal to 7.7 \AA based on Table 1. One may infer that the double-walled structure is preserved. Unlike SW-INTs, DW-GeOH nanotubes do not collapse and maintain their double-walled structure but their shape is no longer cylindrical. Furthermore, the effect of the filling or not of the internal pores by the two different PTM is negligible in comparison with SW-GeOH INTs, which shows that DW-INTs are more rigid radially than SW-INTs.

To summarize, changes of the nanotube morphology have been assessed by following the evolution of the scattering modulations at low Q wavevector values as a function of the pressure. Attenuation of modulation intensities corresponds to deformations of nanotubes from the cylindrical to an ovalized shape. The disappearance of the modulations at a pressure P_c defines the nanotube radial collapse onset which is only evidenced in isolated SW nanotubes. It clearly appears that DW-GeOH is more rigid radially and does not collapse in the pressure range measured, whereas radial collapse onset occurs at $P_c = 1.8$ and 3.5 GPa depending on the PTM used for SW-GeOH and 4 GPa for SW-GeCH₃ compound (Table 2).

Table 2. Values of the Collapse Pressure P_c Measured in the Pressure Range 0–7 GPa and Values of the Axial Young Modulus Y for Aluminogermanate Imogolite Nanotubes

	P_c (GPa)	Y (GPa)
SW-GeOH	1.8 (Si-oil PTM) 3.5 (alcohol PTM)	400
SWb-GeOH	6	600
DW-GeOH		440
SW-GeCH ₃	4	200

Like the modulations located below $Q < 1 \text{ \AA}^{-1}$ discussed above, the broad modulation around 1.8 \AA^{-1} is also a benchmark of the tubular shape of nanotubes, since it does not exist for the unrolled structure (Figure 1). Its evolution as a function of the pressure is plotted in Figure 5 for the four aluminogermanate INT samples. Its intensity decreases as soon as the nanotube cross-sectional shape departs from a circular shape. However, some differences can be noticed between compounds. Concerning DW-GeOH, the intensity of the modulation decreases monotonically and linearly up to 7 GPa, whatever

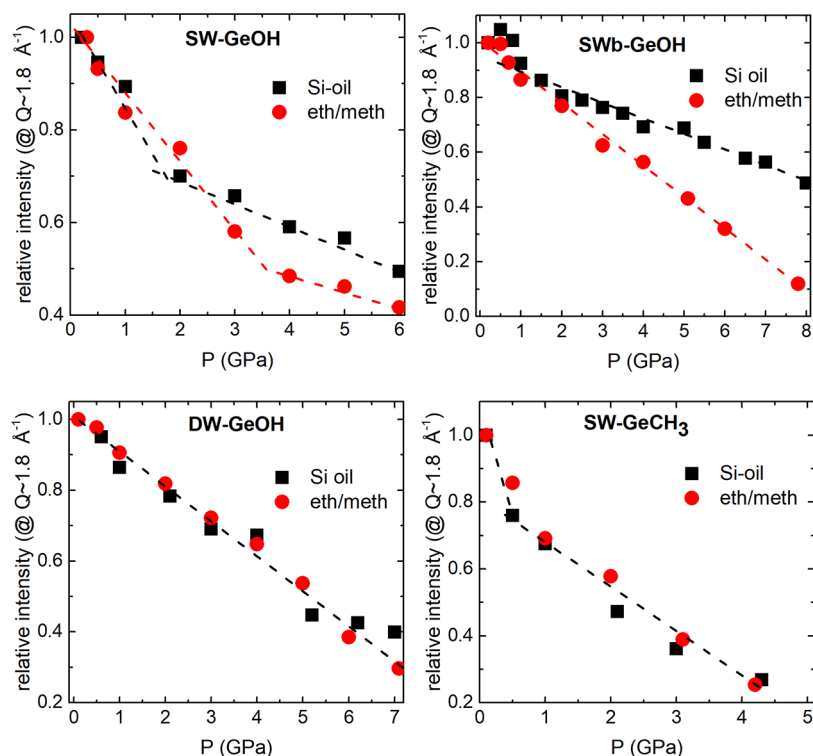


Figure 5. Variation in intensity as a function of the pressure of the modulation located around $Q = 1.8 \text{ \AA}^{-1}$ with pressure-transmitting medium Si oil (black squares) or an ethanol/methanol mixture (red circles). Dashed lines are guides for the eyes.

the type of PTM. The same behavior is also observed for SW-GeCH₃ for pressures above 0.5 GPa, after an initial sharp decrease. This confirms that there is no differential effect of PTM in these two compounds. In contrast, a change of slope in the pressure-dependent variation of intensity is observed for SW-GeOH, at around 1.8 and 3.5 GPa with Si-oil and alcohol PTM respectively, confirming values of the radial collapse onset pressure P_c determined from the evolution of the modulations at $Q < 1 \text{ \AA}^{-1}$. Considering SWb-OH nanotubes, the decrease in intensity is monotonous and linear for both PTM, highlighting the role of the organization of INTs that will be discussed further in the next section. In addition, a smaller variation is observed above 2 GPa with the Si-oil PTM, indicating that the stronger deformations occur mainly at low pressure due to the different filling of the inner cavity of the nanotube in comparison with the alcohol PTM.

Role of the Organization of INTs. SW-GeOH nanotubes can assemble in large bundles and organize on a 2D hexagonal lattice in the plane perpendicular to their long axis.¹⁹ The XRS diagram at $Q < 1 \text{ \AA}^{-1}$ shows narrow diffraction peaks indexed by two Miller indices h and k (see Figure 2), with positions located at

$$Q_{hk} = \sqrt{h^2 + k^2 + hk} \frac{4\pi}{\sqrt{3}a} \quad (1)$$

with a being the hexagonal lattice parameter. Equation 1 is only valid for large bundles,^{19,34} as is the case for SWb-INTs we have studied, with around 60 tubes per bundle. Therefore, the lattice parameter a can be straightforwardly derived by a linear regression fitting of the positions of the observed diffraction peaks ($hk = 10, 11, 20, 21$), which progressively disappear while pressure increases up to $P = 4$ GPa. Pressure-dependent variations of the lattice parameter a are plotted in Figure 6. The lattice constant a is found to be equal to 39.85 Å at 0.2 GPa for

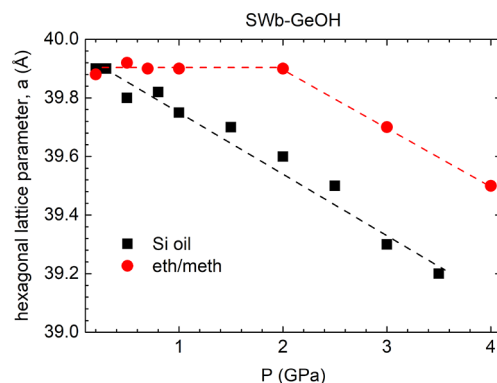


Figure 6. Pressure dependence of the hexagonal lattice parameter a in SWb-GeOH, with the pressure-transmitting medium Si-oil (black squares) or an ethanol/methanol mixture (red circles).

both PTM. When the pressure is increased, the lattice parameter remains constant up to 2 GPa with a for the ethanol/methanol PTM then decreasing to around 39.5 Å at 4 GPa whereas it decreases continuously with Si oil PTM, reaching a lower value of 39.2 Å. Moreover, the magnitude of the variation of the lattice parameter is larger with Si oil than with ethanol/methanol PTM. This is probably due to the filling of the inner cavities of SW-GeOH nanotubes by alcohol molecules, which limits the pressure effect on 2D organization on the hexagonal lattice up to $P = 2$ GPa.

Let us underline that values of the lattice parameter are smaller than the distance between two adjacent cylindrical nanotubes ($2R_c = 40.6 \text{ \AA}$), indicating a polygonization of the nanotubes, as was also demonstrated for single-walled carbon nanotube bundles under high pressures of up to 5 GPa.¹⁰ In previous work with a powder of SWb-GeOH nanotubes heated

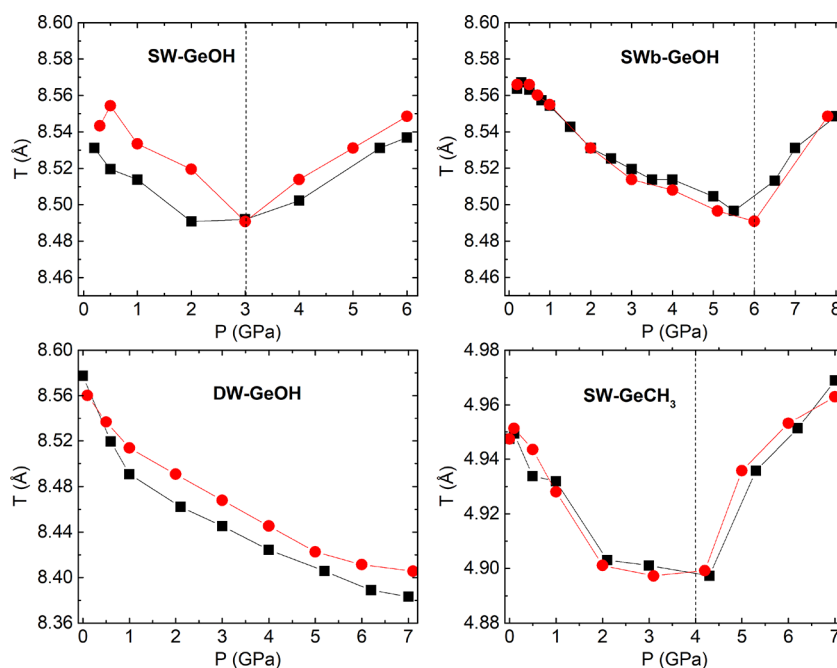


Figure 7. Dependence of the period T upon pressure for the four different Ge-INTs with the transmitting medium Si oil (black squares) or an ethanol/methanol mixture (red circles). Vertical dashed lines are guides for the eye to determine the axial compression to relaxation transition pressure.

at 250 °C, the authors evidenced the hexagonalization of large bundles (around 60 tubes),³¹ where the lattice constant was found to be equal to $a = 39.7$ Å. From our pressure measurements, one can safely state that SWb-GeOH nanotubes assembled in large bundles adopt a hexagonal cross-sectional shape at the lowest pressure applied ($P = 0.2$ GPa), which is progressively deformed when the pressure increases until reaching $P = 4$ GPa. Thereafter, diffraction peaks at $Q < 1$ Å⁻¹ are no longer observable, as the organization is too strongly perturbed. Moreover, the pressure effect is stronger with the Si oil than with the alcohol PTM, which can be ascribed to the different filling of the internal pore of the nanotube. At higher pressures, two peaks are observed at $Q \approx 0.17$ and 0.35 Å⁻¹, which can be attributed to the formation of a lamellar phase. Some noncollapsed SW-GeOH nanotubes are expected to remain, thanks to the protecting effect of the bundling, which may act as spacers between lamellar regions, in a way similar to the mechanism described previously for GeCH₃-INTs.

Axial Compression of INTs. The pressure-induced effect along the nanotube axis is assessed by following the variation of position of the inflection point of the rising edge of the Q_{002} peak related to the axial nanotube period T . The results are reported in Figure 7. At first, a decrease of the period is observed in the four samples, which corresponds to the axial contraction of the nanotubes under pressure. Thereafter, the period increases for all SW INTs, but not for DW INTs. The change occurs at a different pressure values depending on the type of compound, at $P \approx 2$ –3 GPa (depending on the PTM) for SW-GeOH, $P \approx 6$ GPa for SWb-GeOH, and $P \approx 4$ GPa for SW-GeCH₃. This can be described as the transition from a compression regime to a relaxation regime, which is related to a strong structural change in SW INTs. This would correspond to the passage from the cylindrical to an ovalized or polygonized cross-sectional area shape and then to a flattened form of the nanotube under pressure. Indeed, the pressure values at which the axial compression–relaxation transition occurs roughly correlates to the nanotube’s radial collapse onset pressure P_c determined for

SW-GeOH and SW-GeCH₃. The higher value of the transition observed for SWb-GeOH ($P_c = 6$ GPa) underlines the role of the nanotube bundling in the limitation of the pressure effect and corresponds also to the appearance of the lamellar phase. In contrast, the period of DW INTs decreases monotonically with pressure up to 7 GPa, which confirms that no radial collapse of DW-GeOH occurred in this pressure range. The maximum magnitude of the variation ΔT is about -1% for SW INTs ($\Delta T \approx -0.6\%$ for SW-GeOH, -0.8% for SWb-GeOH, -1.2% for SW-GeCH₃) whereas it is slightly larger for DW INTs ($\Delta T \approx -1.6$ to 1.8%).

Within the compression regime, it is possible to fit the axial compressibility ($1/Y$) of the nanotube under hydrostatic pressure using the linear relation $P = Y \frac{T - T_0}{T_0}$, where T is the period at the pressure P (T_0 is the value at ambient pressure), and Y is a constant. Y can be viewed as a pseudo-Young’s modulus if we neglect the contribution from the shear modulus G and the radial Young’s modulus via the Poisson ratios. By analogy with CNTs, this approximation would give the correct order of magnitude, as the Poisson ratio is estimated to be around 0.1⁴⁶ and the shear modulus G is typically 2–3 orders of magnitude lower than the Young’s modulus.⁴⁷ Values of the pseudo-Young’s modulus derived are given in Table 2. They are found to be in the range of 200–600 GPa, of the same order as in the simulations.^{21,26,27} The smallest value (200 GPa) is found for SW-GeCH₃ nanotubes. The value is slightly larger for DW-GeOH (440 GPa) than for SW-GeOH (400 GPa). On the other hand, the stiffness is significantly increased to 600 GPa for SWb-GeOH, which is attributed to the bundling effect and to the polygonization of the nanotube shape.

Long-range order along the nanotube axis can be assessed by the presence of a 004 peak for GeOH INTs. This peak is not observed for SW-GeCH₃ nanotubes, as expected from calculations (Figure 1). A decrease in the intensity of the 004 peak under pressure is effective at 3 and 4 GPa with Si oil and alcohol PTM, respectively, for SW-GeOH (see Figure 2). The

004 peak is still visible at higher pressures for SWb-GeOH, which emphasizes again the role of the bundling organization of the nanotubes in the limitation of the pressure effect. For DW-GeOH, no difference is observed between the two PTM, as the 004 peak is still clearly present at the highest pressure measured ($P = 7$ GPa). This feature confirms that the structure of DW INTs is less affected by the applied pressure than for SW INTs.

Local Deformation around the Ge Atom. In order to have local information on the deformation around the Ge site, we performed XANES experiments under pressures of up to 10 GPa at the Ge K edge (11103 eV). The spectra are reported for both PTM in Figure 8. For all samples and PTM, we observe a

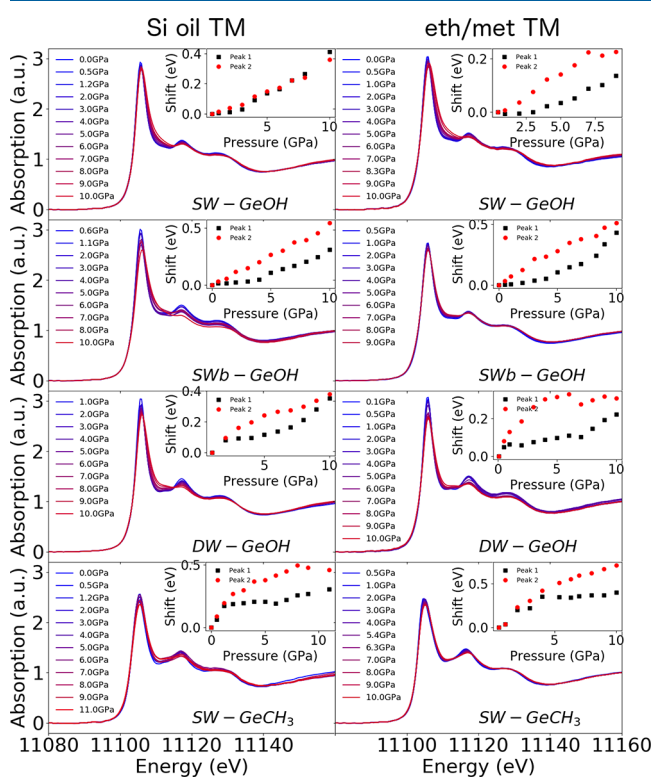


Figure 8. XANES spectra under pressure for the different PTM: Si oil (left) and ethanol/methanol mixture (right). Insets show the evolution of the position of the first (black squares) and second (red circles) peaks at 11105 and 11116 eV, respectively, for each sample and PTM.

general shift of the spectra toward the higher energies, combined with a broadening of the main features, in particular the two main peaks at 11105 and 11116 eV. The shift of both peaks is reported in the insets of Figure 8 as a function of the pressure. Their positions have been determined by a Gaussian function and linear background fit within 5 eV around the peak position. The absence of major changes in the spectral shape suggests that the environment around the Ge site is not significantly modified. The general high-energy shift is expected under pressure because the interatomic distances are reduced, as observed in other systems.⁴⁸ The broadening of the features can be interpreted as a distribution of Ge sites with different interatomic distances due to nonequivalent distortion depending on the position on the tube. As we can observe, there is a larger systematic broadening with Si oil than with the alcohol mixture, suggesting that the tube is deformed at smaller pressure with the former than with the latter. This corroborates the general conclusion of the XRS results. In order to be more

quantitative, we performed an *ab initio* simulation of the XANES spectra using the FDMNES code.⁴⁹ We simulated the XANES spectra using the Green's function method, with a cluster radius of 5 Å around the absorbing atom, corresponding to 220 atoms. To simulate the effect of pressure, spectra were calculated based on the refined atomic positions,^{25,37} applying both radial and axial compressions from 0 to 1.2%. The result is reported in Figure 9. Simulations reproduce the shape of the experimentally

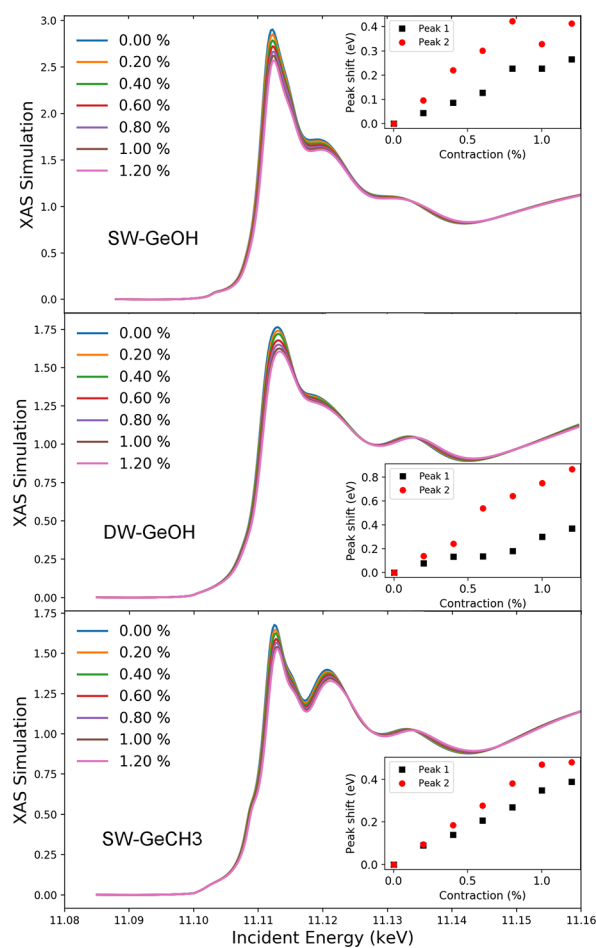


Figure 9. XANES spectra simulated with a cluster of 5 Å using the FDMNES code for contracted tubes, with contraction ranging from zero to 1.2%. Insets show the evolution of the position of the first and second peaks at 11105 and 11116 eV, respectively.

observed spectra, with the three main peaks. While the quantitative agreement is not perfect, in particular with the calculated second peaks closer to the first peaks than in the experimental spectra, the qualitative similitude is high enough to allow us further comparison. We thus fitted the position of the first two peaks the same way we did for experimental spectra. The evolution as a function of nanotube contraction is represented in the insets of Figure 9. This comparison remains valid only in the compression regime where the period T decreases. This restricts its application to the 0–4, 0–7, and 0–4 GPa ranges for SW-GeOH, DW-GeOH, and SW-GeCH₃ respectively (see Figure 6). We will then compare the contraction between 0 and 4 GPa for all three structures. For the SW-GeOH, we see that the experimental shifts of the first and second peaks are approximately 0.1 and 0.2 eV, respectively, at 4 GPa. Comparing with the simulation, we can

deduce that the contraction exceeds 0.4%. For the SW-GeCH₃, there is a slight difference between PTM: for Si oil the shifts are 0.2 and 0.4 eV for the first and second peaks, respectively, and 0.3 and more than 0.4 eV for the alcohol mixture, respectively. This would correspond to a contraction of above 0.6% for both PTM. In this isotropic compression model, the XANES measurements and simulations thus confirm the relative compressibility of the different SW INTs deduced from the XRS experiments. Concerning the DW-GeOH, we can see that the shifts do not exceed 0.1 and 0.2 eV at 4 GPa for the first and second peaks, respectively, leading to an estimation of contraction of less than 0.2%. This is also confirmed qualitatively with the XRS results: SW-INTs ($Y = 200$ and 400 GPa) are more compressible than DW nanotubes ($Y = 440$ GPa). It also corroborates the intuitive guess that DW-INTs are more rigid and have a larger bulk modulus than the SW-INTs. Being more quantitative would be speculative, due to the fact that we know INTs are quickly deformed and are no longer cylindrical under pressure, limiting the relevance of the comparison to simulations. The qualitative agreement with the axial compressibility hierarchy determined by XRS, however, remains very compelling.

CONCLUSION

In this study, radial-pressure-induced deformations of aluminogermanate imogolite nanotubes (INTs) have been evidenced depending on the morphology, organization, or functionalization of the internal cavity of INTs, while the local structure, in the environment of the germanium atom, is not much altered. Ovalization of the nanotube cross-sectional shape occurs for isolated single-walled INTs, whereas they are hexagonalized when organized into large bidimensional crystalline bundles. Radial collapse onset pressures have been determined for single-walled INTs. In addition, the radial collapse of the SW-GeOH nanotube structure was shown to depend on the pressure-transmitting medium used and on the organization of the nanotubes. On the other hand, although double-walled INTs also deform by ovalizing, the double-walled structure does not collapse and is preserved within the measured pressure range. Finally, these experiments allow the first experimental determination of the axial Young's modulus of aluminogermanate imogolite nanotubes. Our results should certainly stimulate new theoretical and experimental studies for an understanding of the physical properties of imogolite nanotubes and for the development of new nanomaterials.

AUTHOR INFORMATION

Corresponding Authors

S. Rouzière – Université Paris-Saclay, CNRS, Laboratoire de Physique des Solides, 91405 Orsay cedex, France;

orcid.org/0000-0002-1190-2275;

Email: stephan.rouziere@universite-paris-saclay.fr

V. Balédent – Université Paris-Saclay, CNRS, Laboratoire de Physique des Solides, 91405 Orsay cedex, France;

orcid.org/0000-0002-9437-434X;

Email: victor.baledent@universite-paris-saclay.fr

Authors

E. Paineau – Université Paris-Saclay, CNRS, Laboratoire de Physique des Solides, 91405 Orsay cedex, France;

orcid.org/0000-0002-6776-7201

E. Elkaim – Synchrotron SOLEIL, 91192 Gif-sur-Yvette, France

T. Bizien – Synchrotron SOLEIL, 91192 Gif-sur-Yvette, France

L. Nataf – Synchrotron SOLEIL, 91192 Gif-sur-Yvette, France

Y. Pan – Université Paris-Saclay, CNRS, Laboratoire de Physique des Solides, 91405 Orsay cedex, France

P. Launois – Université Paris-Saclay, CNRS, Laboratoire de Physique des Solides, 91405 Orsay cedex, France

Complete contact information is available at:

<https://pubs.acs.org/10.1021/acs.inorgchem.2c03798>

Notes

The authors declare no competing financial interest.

ACKNOWLEDGMENTS

We acknowledge SOLEIL for provision of synchrotron beam times (proposal numbers 20191353, 20210185, and 20210305) on the SWING, CRISTAL, and ODE beamlines. Y.P. acknowledges financial support by the China Scholarship Council (CSC, No. 202106190044).

REFERENCES

- (1) De Volder, M. F. L.; Tawfick, S. H.; Baughman, R. H.; Hart, A. J. Carbon Nanotubes: Present and Future Commercial Applications. *Science* **2013**, *339*, 535–539.
- (2) Anantram, M.; Léonard, F. Physics of carbon nanotube electronic devices. *Rep. Prog. Phys.* **2006**, *69*, 507–561.
- (3) Park, H. G.; Jung, Y. Carbon nanofluidics of rapid water transport for energy applications. *Chem. Soc. Rev.* **2014**, *43*, 565–576.
- (4) Marcotte, A.; Mouterde, T.; Niguès, A.; Siria, A.; Bocquet, L. Mechanically activated ionic transport across single-digit carbon nanotubes. *Nat. Mater.* **2020**, *19*, 1057–1061.
- (5) Weng, B.; Liu, S.; Tang, Z.-R.; Xu, Y.-J. One-Dimensional Nanostructure Based Materials for Versatile Photocatalytic Applications. *Rsc. Adv.* **2014**, *4*, 12685–12700.
- (6) Ge, M.; Li, Q.; Huang, J.; Li, S.; Zhang, Z.; Chen, K.; Zhang, S.; Al-Deyab, S.; Lai, Y. One-dimensional TiO₂ Nanotube Photocatalysts for Solar Water Splitting. *Adv. Sci.* **2017**, *4*, 1600152.
- (7) Treacy, M.; Ebbesen, T.; Gibson, J. Exceptionally high Young's modulus observed for individual carbon nanotubes. *Nature* **1996**, *381*, 678–680.
- (8) Hernandez, E.; Goze, C.; Bernier, P.; Rubio, A. Elastic Properties of Single-Wall Nanotubes. *Appl. Phys. A: Mater. Sci. Process.* **1999**, *68*, 287–292.
- (9) Tang, J.; Qin, L.-C.; Sasaki, T.; Yudasaka, M.; Matsushita, A.; Iijima, S. Compressibility and polygonization of single-walled carbon nanotubes under hydrostatic pressure. *Phys. Rev. Lett.* **2000**, *85*, 1887.
- (10) Rols, S.; Goncharenko, I.; Almirac, R.; Sauvajol, J.; Mirebeau, I. Polygonization of single-wall carbon nanotube bundles under high pressure. *Phys. Rev. B* **2001**, *64*, 153401.
- (11) San Miguel, A. Nanomaterials under high-pressure. *Chem. Soc. Rev.* **2006**, *35*, 876–889.
- (12) Silva-Santos, S.; Alencar, R.; Aguiar, A.; Kim, Y.; Muramatsu, H.; Endo, M.; Blanchard, N.; San Miguel, A.; Souza Filho, A. From high pressure radial collapse to graphene ribbon formation in triple-wall carbon nanotubes. *Carbon* **2019**, *141*, 568–579.
- (13) Elliott, J.; Poli, E.; Scivetti, I.; Ratcliff, L.; Andrinopoulos, L.; Dziedzic, J.; Hine, N.; Mostofi, A.; Skylaris, C.-K.; Haynes, P.; Teobaldi, G. Chemically Selective Alternatives to Photoferroelectrics for Polarization-Enhanced Photocatalysis: The Untapped Potential of Hybrid Inorganic Nanotubes. *Advanced Science* **2017**, *4*, 1600153.
- (14) Kang, D.-Y.; Brunelli, N.; Yucelen, G.; Venkatasubramanian, A.; Zang, J.; Leisen, J.; Hesketh, P.; Jones, C.; Nair, S. Direct synthesis of single-walled aluminosilicate nanotubes with enhanced molecular adsorption selectivity. *Nature Commun.* **2014**, *5*, 3342.
- (15) Cradwick, P. D. G.; Farmer, V. C.; Russell, J. D.; Masson, C. R.; Wada, K.; Yoshinaga, N. Imogolite, a Hydrated Aluminum Silicate of Tubular Structure. *Nature Phys. Sci.* **1972**, *240*, 187–189.
- (16) Yoshinaga, N.; Aomine, S. Imogolite in some ando soils. *Soil Sci. Plant Nutr.* **1962**, *8*, 22–29.

- (17) Farmer, V. C.; Fraser, A. R.; Tait, J. M. Synthesis of imogolite: a tubular aluminium silicate polymer. *J. Chem. Soc. Chem. Commun.* **1977**, 13, 462–463.
- (18) Amara, M.-S.; Paineau, E.; Bacia-Verloop, M.; Krapf, M.-E. M.; Davidson, P.; Belloni, L.; Levard, C.; Rose, J.; Launois, P.; Thill, A. Single-step formation of micron long (OH)3Al2O3Ge(OH) imogolite-like nanotubes. *Chem. Commun.* **2013**, 49, 11284–11286.
- (19) Paineau, E.; Amara, M.; Monet, G.; Peyre, V.; Rouzière, S.; Launois, P. Effect of Ionic Strength on the Bundling of Metal Oxide Imogolite Nanotubes. *J. Phys. Chem. C* **2017**, 121, 21740–21749.
- (20) Konduri, S.; Mukherjee, S.; Nair, S. Strain energy minimum and vibrational properties of single-walled aluminosilicate nanotubes. *Phys. Rev. B* **2006**, 74, 033401.
- (21) Guimaraes, L.; Enyashin, A. N.; Frenzel, J.; Heine, T.; Duarte, H. A.; Seifert, G. Imogolite nanotubes: stability, electronic, and mechanical properties. *ACS Nano* **2007**, 1, 362–368.
- (22) Maillet, P.; Levard, C.; Spalla, O.; Masion, A.; Rose, J.; Thill, A. Growth Kinetic of Single and Double-Walled Aluminogermanate Imogolite-like Nanotubes: An Experimental and Modeling Approach. *Phys. Chem. Chem. Phys.* **2011**, 13, 2682–2689.
- (23) Bottero, I.; Bonelli, B.; Ashbrook, S.; Wright, P.; Zhou, W.; Tagliabue, M.; Armandi, M.; Garrone, E. Synthesis and characterization of hybrid organic/inorganic nanotubes of the imogolite type and their behaviour towards methane adsorption. *Phys. Chem. Chem. Phys.* **2011**, 13, 744–750.
- (24) Amara, M.-S.; Paineau, E.; Rouzière, S.; Guiose, B.; Krapf, M.-E. M.; Taché, O.; Launois, P.; Thill, A. Hybrid, Tunable-Diameter, Metal Oxide Nanotubes for Trapping of Organic Molecules. *Chem. Mater.* **2015**, 27, 1488–1494.
- (25) Monet, G.; Amara, M.-S.; Rouzière, S.; Paineau, E.; Chai, Z.; Elliott, J.; Poli, E.; Liu, L.-M.; Teobaldi, G.; Launois, P. Structural resolution of inorganic nanotubes with complex stoichiometry. *Nature Commun.* **2018**, 9, 2033.
- (26) Lourenco, M.; Guimaraes, L.; Da Silva, M.; de Oliveira, C.; Heine, H.; Duarte, H. Nanotubes with Well-Defined Structure: Single- and Double-Walled Imogolites. *J. Phys. Chem. C* **2014**, 118, 5945–5953.
- (27) Liou, K.-H.; Tsou, N.-T.; Kang, D.-Y. Relationships among the structural topology, bond strength, and mechanical properties of single-walled aluminosilicate nanotubes. *Nanoscale* **2015**, 7, 16222–16229.
- (28) Konduri, S.; Mukherjee, S.; Nair, S. Controlling nanotube dimensions: correlations between composition, diameter, and internal energy of single-walled mixed oxide nanotubes. *ACS Nano* **2007**, 1, 393–402.
- (29) Tamura, K.; Kawamura, K. Molecular dynamics modeling of tubular aluminum silicate: imogolite. *J. Phys. Chem. B* **2002**, 106, 271–278.
- (30) Creton, B.; Bougeard, D.; Smirnov, K.; Guilment, J.; Poncelet, O. Molecular dynamics study of hydrated imogolite. Structure and dynamics of confined water. *Phys. Chem. Chem. Phys.* **2008**, 10, 4879–4888.
- (31) Amara, M.-S.; Rouzière, S.; Paineau, E.; Bacia-Verloop, M.; Thill, A.; Launois, P. Hexagonalization of Aluminogermanate Imogolite Nanotubes Organized into Closed-Packed Bundles. *J. Phys. Chem. C* **2014**, 118, 9299–9306.
- (32) MacKenzie, K.; Bowden, M.; Brown, J.; Meinhold, R. Structure and thermal transformation of imogolite studied by ²⁹Si and ²⁷Al high-resolution solid-state nuclear magnetic resonance. *Clay Clay Miner* **1989**, 37, 317–324.
- (33) Zanzottera, C.; Vicente, A.; Armandi, M.; Fernandez, C.; Garrone, E.; Bonelli, B. Thermal Collapse of Single-Walled Aluminosilicate Nanotubes: Transformation Mechanisms and Morphology of the Resulting Lamellar Phases. *J. Phys. Chem. C* **2012**, 116, 23577–23584.
- (34) Rouzière, S.; Amara, M.; Paineau, E.; Launois, P. Deformations and Thermal Modifications of Imogolite. *Developments in Clay Science* **2016**, 7, 254–278.
- (35) Monet, G.; Rouzière, S.; Vantelon, D.; Coelho Diogo, C.; Maurin, D.; Bantignies, J.-L.; Launois, P.; Paineau, E. Mechanisms of Structural Reordering During Thermal Transformation of Aluminogermanate Imogolite Nanotubes. *J. Phys. Chem. C* **2021**, 125, 12414–12423.
- (36) Paineau, E.; Rouzière, S.; Monet, G.; Coelho-Diogo, C.; Morfin, I.; Launois, P. Role of initial precursors on the liquid-crystalline phase behavior of synthetic aluminogermanate imogolite nanotubes. *J. Colloid Interface Sci.* **2020**, 580, 275–285.
- (37) Monet, G.; Paineau, E.; Chai, Z.; Amara, M.; Orecchini, A.; Jimenez-Ruiz, M.; Ruiz-Caridad, A.; Fine, L.; Rouzière, S.; Liu, L.-M.; Teobaldi, G.; Rols, S.; Launois, P. Solid wetting-layers in inorganic nano-reactors: the water in imogolite nanotube case. *Nanoscale Adv.* **2020**, 2, 1869.
- (38) Paineau, E.; Krapf, M.-E.; Amara, M.-S.; Matskova, N.; Dozov, I.; Rouzière, S.; Thill, A.; Launois, P.; Davidson, P. A liquid-crystalline hexagonal columnar phase in highly-dilute suspensions of imogolite nanotubes. *Nature Commun.* **2016**, 7, 10271.
- (39) Robertson, D. H.; Brenner, D. W.; Mintmire, J. W. Energetics of nanoscale graphitic tubules. *Phys. Rev. B* **1992**, 45, 12592.
- (40) Chijioke, A. D.; Nellis, W. J.; Soldatov, A.; Silvera, I. F. The ruby pressure standard to 150 GPa. *J. Appl. Phys.* **2005**, 98, 114905.
- (41) Tateiwa, N.; Haga, Y. Evaluations of pressure-transmitting media for cryogenic experiments with diamond anvil cell. *Rev. Sci. Instrum.* **2009**, 80, 123901.
- (42) Cosgrove, T.; Swier, S.; Schmidt, R. G.; Muangpil, S.; Espidel, Y.; Griffiths, P. C.; Prescott, S. W. Impact of End-Tethered Polyhedral Nanoparticles on the Mobility of Poly(dimethylsiloxane). *Langmuir* **2015**, 31, 8469–8477.
- (43) Bousige, C.; Rols, S.; Paineau, E.; Rouzière, S.; Mocuta, C.; Verbeck, B.; Wright, J.; Kataura, H.; Launois, P. Progressive melting in confined one-dimensional C60 chains. *Phys. Rev. B* **2012**, 86, 045446.
- (44) Baudalet, F.; Kong, Q.; Nataf, L.; Cafun, J. D.; Congeduti, A.; Monza, A.; Chagnot, S.; Itié, J. P. ODE: A new beam line for high-pressure XAS and XMCD studies at SOLEIL. *High Pressure Res.* **2011**, 31, 136–139.
- (45) Cambedouzou, J.; Chorro, M.; Almairac, R.; Noé, L.; Flahaut, E.; Rols, S.; Monthieux, M.; Launois, P. X-Ray Diffraction as a Tool for the Determination of the Structure of Double-Walled Carbon Nanotube Batches. *Phys. Rev. B* **2009**, 79, 195423.
- (46) Chen, W.; Cheng, H.; Liu, Y. Radial mechanical properties of single-walled carbon nanotubes using modified molecular structure mechanics. *Comput. Mater. Sci.* **2010**, 47, 985–993.
- (47) Salvétat, J.-P.; Briggs, G.; Bonard, J.-M.; Bacs, R.; Kulik, A.; Stöckli, T.; Burnham, N.; Forró, L. Elastic and Shear Moduli of Single-Walled Carbon Nanotube Ropes. *Phys. Rev. Lett.* **1999**, 82, 944.
- (48) Balédent, V.; Rullier-Albenque, F.; Colson, D.; Ablett, J. M.; Rueff, J. P. Electronic properties of BaFe2As2 upon doping and pressure: The prominent role of the As p orbitals. *Phys. Rev. Lett.* **2015**, 114, 1–5.
- (49) Joly, Y.; Cavallari, C.; Guda, S. A.; Sahle, C. J. Full-Potential Simulation of X-ray Raman Scattering Spectroscopy. *J. Chem. Theory Comput.* **2017**, 13, 2172–2177.